Exp Fluids (2014) 55:1684
DOI 10.1007/s00348-014-1684-x

RESEARCH ARTICLE

Color-coded three-dimensional micro particle tracking velocimetry and application to micro backward-facing step flows

Wei-Hsin Tien · Dana Dabiri · Jay R. Hove

Received: 1 November 2012 / Revised: 30 June 2013 / Accepted: 29 January 2014

Abstract In this work, the authors proposed a microscopic particle tracking system based on the previous work (Tien et al. in Exp Fluids 44(6):1015–1026, 2008). A three-pinhole plate, color-coded by color filters of different wavelengths, is utilized to create a triple exposure pattern on the image sensor plane for each particle, and each color channel of the color camera acts as an independent image sensor. This modification increases the particle image density of the original monochrome system by three times and eliminates the ambiguities caused by overlap of the triangle exposure patterns. A novel lighting method and a color separation algorithm are proposed to overcome the measurement errors due to crosstalk between color filters. A complete post-processing procedure, including a cascade correlation peak-finding algorithm to resolve overlap particles, a calibration-based method to calculate the depth location based on epipolar line search method, and a vision-based particle tracking algorithm is developed to identify, locate and track the Lagrangian motions of the tracer particles and reconstruct the flow field. A 10X infinity-corrected microscope and back-lighted by three individual high power color LEDs aligning to each of the pinhole is used to image the flow. The volume of imaging is $600 \times 600 \times 600$ μm^3. The experimental uncertainties of the system verified with experiments show that the location uncertainties are less than 0.10 and 0.08 μm for the in-plane and less than 0.82 μm for the out-of-plane components, respectively. The displacement uncertainties are 0.62 and 0.63 μm for the in-plane and 0.77 μm for the out-of-plane components, respectively. This technique is applied to measure a flow over a backward-facing micro-channel flow. The channel/step height is 600/250 μm. A steady flow with low particle density and an accelerating flow with high particle density are measured and compared to validate the flow field resolved from a two-frame tracking method. The Reynolds number in the current work varies from 0.033 to 0.825. A total of 20,592 vectors are reconstructed by time-averaged tracking of 156 image pairs from the steady flow case, and roughly 400 vectors per image pair are reconstructed by two-frame tracking from the accelerating flow case.

1 Introduction

Particle tracking velocimetry (PTV), like its counterpart, particle image velocimetry (PIV) are a whole field measurement technique for measuring flow velocities in fluid mechanics studies. Both are non-intrusive and capable of measuring the whole flow field simultaneously. These techniques have been improved to meet the requirements of various applications, yet they are still evolving to become a better tool for the researchers to use in many advanced studies. One of the most active areas in recent years is the micro-PIV/PTV, where the techniques are used to imaging the micro-scale flow phenomenon. The first micro-PIV was developed by Santiago et al. (1998) to image a Hale-Shaw flow around a 30-micrometer elliptical cylinder, which was

This article is part of the Topical Collection on Application of Laser Techniques to Fluid Mechanics 2012.

W.-H. Tien · D. Dabiri (✉)
Department of Aeronautics and Astronautics,
University of Washington, Seattle, WA, USA
e-mail: dabiri@aa.washington.edu

J. R. Hove
Department of Molecular and Cellular Physiology,
University of Cincinnati, Cincinnati, OH, USA

Published online: 27 February 2014

a direct implementation from a macro-scale 2D plane PIV system to a micro-scale system. In the study, epifluorescence microscopy was used to image the tracer particles, and a volumetric illumination from a white light source was used. The velocity fields were measured with spatial resolution down to 6.9 μm × 6.9 μm × 1.5 μm. Most of the 2D micro-PIV/PTV systems use a similar experimental setup, with various data processing techniques to reconstruct the flow field.

The main limitation of the 2D planar PIV/PTV system is that it only measures a slice of the flow with the two coplanar velocity components (2D-2C). A 3D-3C technique to break the limitation to resolve more complex flow is therefore a goal for many researchers. PTV is more favored than PIV since most of the 3D techniques are point-based method, which means each particle location has to be calculated before resolving the flow field, making PTV a natural choice for the 3D techniques. Furthermore, one of the advantages of PTV in micro-scale flow over PIV is that higher resolution can be achieved with the same particle density. PIV requires 6–10 particle images in one interrogation window to resolve one reliable velocity vector, while PTV produces a velocity vector from each the particle image. For macro-scale flow, it is not an issue since higher particle concentrations can be achieved and PTV method may encounter difficulties in identifying overlapped particle images. However, due to the high magnification and volumetric illumination used in most of the micro-scale PTV applications, the particle image density is limited in order to achieve acceptable signal-to-noise ratio. As a result, the resolution of PIV is usually lower than PTV methods.

Several 3D techniques have been developed to overcome 2D limitation. Stereoscopy techniques (Lindken et al. 2006; Bown et al. 2006) acquire images from two viewing angles and reconstruct the velocity components from the displacements found in the two image planes. With proper calibration, the system can achieve high accuracy. The disadvantage of the technique for micro-applications is that a low numerical aperture lens (NA) is required for the stereo microscope objective lens as opposed to a traditional high NA objective lens, which limits the spatial resolution of the images. Another limitation is that this technique can only measure out-of-plane velocity components in a planar region (2D-3C); thus, a scanning procedure throughout the entire volume of interest is required to achieve a volumetric measurement (3D-3C). Digital holographic microscopy (DHM, Sheng et al. 2006; Satake et al. 2006; Ooms et al. 2009) is digital holography applied to microscopy. Instead of recording images of the object space, the image sensor is used to record the scattered and non-scattered light interference patterns as a hologram. Using an objective lens to magnify the hologram, the resolution of the current image sensors can replace the traditional photographic film. The locations of the particles are then numerically reconstructed from the hologram. The technique is proven to be easy to set up, and the main advantage is the achievable high particle density and large measurable depth. The main drawback is that the hologram reconstruction algorithm is very computationally intensive and time-consuming. Wavefront sensing (Angarita-Jaimes et al. 2006; Towers et al. 2006; Chen et al. 2009) and astigmatism particle tracking velocimetry (APTV, Cierpka et al. 2010, 2011) utilize an additional cylindrical lens other than the field lens to the optics to create an anamorphic imaging system. The particle images thus deform differently in the x and y direction when the particle is out of focus, so the lengths of the x and y axes of the elliptical particle image relate to the depth location of the particle uniquely. Compare with other methods, the main advantage of this technique is the ease of changing the size of the measuring depth range by either changing the different focal length of the cylindrical lens or the distance between the cylindrical lens and the spherical lens. The main challenge in this technique is the lower particle image density for each image pair due to particle image overlapping. Defocused techniques using diffraction patterns (Park and Kihm 2006; Peterson et al. 2008; Luo et al. 2006; Luo and Sun 2011) are based on the diffraction effect of the defocused particle image. The defocused particle image form concentric ring structures, which vary in size with the depth distance. Therefore, it is possible to relate the depth location with the diffraction pattern to calculate the particle position. The main advantages of these methods are the high accuracy of the depth location, and no additional optics are required to perform the measurements. The disadvantages include low particle image density (to avoid particle image overlapping) and small measurable depth (because of low signal-to-noise ratios of the defocused particles). The other defocused techniques utilize a multiple-pinhole plate to create multiple exposures of the same particle on the image plane to create a particular pattern. The particle depth location can be calculated by relating the pattern size variation to its depth location. This concept was first proposed by Willert and Gharib (1992), in which a three-pinhole aperture mask is inserted between the image sensor and the measuring volume. Using this mask, any particle away from the focal plane forms triple image exposures on the imaging plane, and the distances between each exposure increases as the actual distance of the particle to the focal plane increases. Thus, the depth location can be calculated based on the size of the triangular pattern formed from the three exposures. The technique is successfully applied to the macro-scale flows by Pereira et al. (2000), Pereira and Gharib (2002). Yoon and Kim (2006) first applied the method to a micro-scale backward-facing step flow. A calibration-based method is proposed later by

Pereira et al. (2007) as an equivalent optical model of the complicated multi-element microscope system to simplify calculations. The main advantage of this technique is the potential to have a better balance between computational cost and particle density. Since the depth calculation is purely based on geometric optics, the requirement for computational power is less than those methods based on diffraction patterns or DHM. The particle image density can also be potentially higher than other methods, except the DHM technique, since the defocused particle image size is smaller. The major disadvantage is the lower optical efficiency due to the use of small pinholes, which significantly reduced the light exposure. In our previous study, Tien et al. (2008) proposed a novel approach using the original three-pinhole single camera system with color camera and a different color filter on each of the pinholes. Using this setup, the particle image exposure is now color-coded, where each color channel acts as an independent image sensor. This modification raised the potential particle image density of the original system by a factor of three and eliminates the ambiguities caused by overlap of the triangle patterns. With a forward-scattering setup, the loss of optical efficiency is largely compensated. Since this system has an excellent potential to resolve flow with high particle density, it is a suitable choice to study unsteady flow phenomenon. In that study, the magnification is increased to 2.39 to image a 3.35 × 2.5 × 1.5 mm volume. 25-μm diameter polystyrene particles are used to image buoyancy driven flow. In addition, an effective single-lens optical model to represent a multi-element lens system is also proposed that results in better measurements. Table 1 shows selected published works of the techniques described above. The basic operational parameters including spatial and temporal resolution, particle size, vectors per image pair, illumination method, magnification and image sensor resolution are listed.

In the present work, the authors propose a microscopic particle tracking system that has the potential of measuring micro-scale flows by two-frame tracking. The system is a miniaturization of previous work (Tien et al. 2008), and modifications are made to resolve the issues encountered in the miniaturization process. To demonstrate the ability of the system, the method is applied to measure an accelerating flow over a backward-facing step in a micro-channel. The system parameters are also listed in Table 1 to compare with the other current methods. The experimental method is described in Sect. 2, including a novel illuminating method, a new color separation algorithm for image pre-processing, and a calibration-based method for calculate the depth location based on epipolar line search method. The experimental setup, calibration and measurement uncertainty are described in Sect. 3. The experimental results of the micro-channel flow are shown and discussed in Sect. 4. Finally, the conclusion and the future work are discussed in Sect. 5.

2 Experimental method

2.1 System principle

The color-coded single-lens 3D digital particle tracking velocimetry system has two features that make it different from DDPIV systems: color-coded pinholes and white light forward-scattering illumination. Figure 1 shows how the defocused particle image (triplet) on the CCD plane is superimposed from the three pinhole apertures. Since black particles are imaged, these particles will block the white light and form particle shadows on the images emerging from each of the red, green and blue filtered pinhole apertures. This modification provides good contrast between the background and the particle images because the forward-scattering illumination provides more light into the CCD sensor. The color-coded pinholes reduce the ambiguity problem of matching the triplets from a monochrome image and raise the achievable particle image density by a factor of three.

To achieve our purpose of imaging micro-scale fluid flow, the system has to be modified to adapt to the changes of image volume size. The biggest change is to increase the modification of the optical system. In the previous work, a 105-mm photographic lens for single-lens reflex camera (SLR) is used with a bellow tube to increase the magnification to 2.69. In the current system, a microscope system is used and the minimum magnification is 10. The huge difference in magnification increases the aberration of the optics, especially the chromatic aberration. The chromatic aberration causes different wavelengths of light to have different focal lengths, and it affects the imaging system in several ways. Thus, modifications are made to adapt the color-coded single-lens defocusing system to be suitable for microscopic applications. Therefore, the modified system is renamed as 3D-μPTV system.

2.2 Illumination method

The color aberration shifts the peak locations of the particle images. The image profile of a particle under illumination produced by a diffraction limited imaging system can be approximated by a Gaussian distribution (Adrian and Westerweel 2011), and the peak location is used to calculate the particle location. A typical spectral response of the pinhole color filters is not a narrow band-pass filter because it is desirable to collect the light as much as possible for an incoherent light source. Therefore, the spectral response of white light passing through a filter is still an

Table 1 List of operating parameters of selected 3D micro PIV/PTV methods

References	Technique	Spatial resolution (PIV)	Temporal resolution	Particle size	Vectors per image pair (PTV)	Illumination	Magnification	Sensor resolution	Measurable depth (μm)
Lindken et al. (2006)	Stereoscopy	44 × 44 × 15 μm	10 μs	0.57 μm	NA	Pulsed laser	9.4	NA	22
Bown et al. (2006)	Stereoscopy	10 × 10 × 10 μm	100 ms	0.91 μm	NA	Pulsed laser	10	1,280 × 1,024	45
Sheng et al. (2006)	DHM	NA	66 ms	3.2 μm	5,679	Continuous laser	10	2,048 × 2,048	1,000
Ooms et al. (2009)	DHM	NA	20 μs	2 μm	366.96	Pulsed laser	10	2,048 × 2,048	1,000
Satake et al. (2006)	DHM	NA	100 μs	1 μm	104	Pulsed laser	40	1,024 × 1,024	92
Chen et al. (2009)	WFS	NA	0.66 ms	2 μm	30	Continuous laser	4	1,280 × 960	600
Cierpka et al. (2010)	APTV	NA	300 μs	5 μm	15	Pulsed laser	20	1,376 × 1,040	90
Park and Kihm (2006)	Diffraction RING	NA	33 ms	0.5 μm	<50	Continuous mercury lamp	40	1,024 × 1,024	25
Peterson et al. (2008)	Diffraction ring	NA	NA	3 μm	2.25	Pulsed laser	40	1,376 × 1,040	50
Pereira et al. (2007)	Pinhole pattern	NA	4 ms	2 μm	<100	Continuous laser	20	512 × 384	150
Yoon and Kim (2006)	Pinhole pattern	NA	1 ms	3 μm	<100	Continuous laser	20	1,280 × 1,024	90
Present work	Pinhole pattern	NA	33 ms	2 μm	444	Continuous LED	10	1,024 × 1,024	600

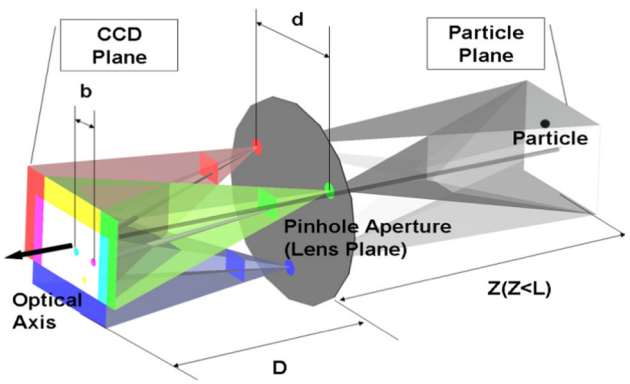

Fig. 1 3D images obtained from a *black* particle illuminated with backlighting from a *white* light source through three *color* filters

integral contains all wavelengths of light, just with a weighting distribution that suppresses wavelengths other than the dominant wavelength of the filter.

For a perfect optical system with no color aberration, the peak location is the same for all wavelengths of light, so the peak calculated from the particle image profile based on the Gaussian shape assumption is accurate. However, with color aberration, the peak location for different wavelengths deviates from each other, as shown in Fig. 2a. Thus, the calculated peak location shifts from the true peak location and contribute to the measurement error of the system (Fig. 2b). The amount of shift is a function of the particle physical location and therefore cannot be corrected without knowing the particle location first.

To resolve this issue without using narrow-band filters and reducing the light intensity, a new configuration of lighting is used for the 3D-μPTV system. As shown in Fig. 3, each pinhole is now aligned with a individual light source with corresponding color to match the spectral response of the color filter on each pinhole. Because the light is from an inclined angle aligned to the corresponding pinhole, the scattering angle of the light to the other two pinholes is significantly redirected away from their former optimized scattering angle ($\approx 0°$). Therefore, only the wavelength of light coming from the matched light source results in the particle image exposure for the corresponding pinhole, and the peak shift due to color aberration can be minimized.

2.3 Color separation

A method for separating the three colors is necessary to identify the color-coded triplet images taken by this system. In theory, this can be easily done if the spectra of each of the red, green and blue color filters perfectly match the

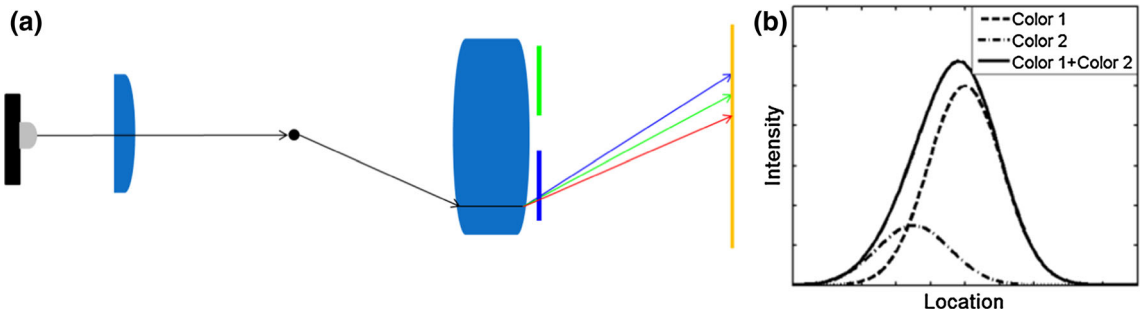

Fig. 2 Particle image peak shifts due to color aberration: **a** *color* aberration due to white light illumination, **b** the skewed Gaussian distribution due to the peak shifts

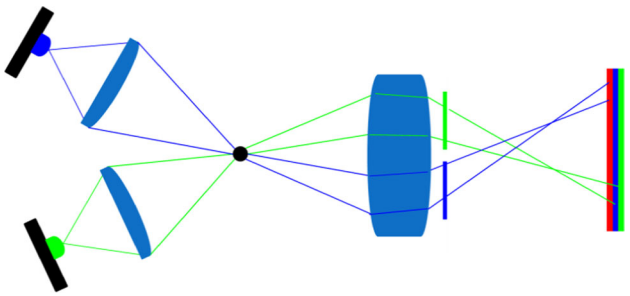

Fig. 3 Proposed illumination configuration

spectra of each of the red, green and blue sensors, respectively, since light emerging from each of the color-filtered pinholes would expose only on their respective sensor. In reality, the spectra of the color filters and the image sensors do not match, thereby causing multiple pinhole exposures on each of the image sensors. Due to the signal crosstalk between the color channels of the image sensor, multiple exposures still happen even a single wavelength light passing through each pinhole. As shown in Fig. 4a, the typical spectral response of the color filters used in a CCD camera shows overlap region between color channels. Wavelengths of light falling in these regions create signal bleed-through to both color channels, thus causing multiple exposure images at the same location through each pinhole with the corresponding single color light source, as shown in Fig. 4b. Thus, a new algorithm to separate the color is developed to resolve this issue.

Eliminating the crosstalk between color channels is equivalent to decorrelating the image data from the color channels. Using principal component transformation (PCT, Richards and Jia 1999), the image data based on the correlated R, G and B primaries can be decorrelated to form a new image based on three independent new primaries. For each pixel of the image, the color can be expressed as

$$\mathbf{C}_{ij} = \begin{bmatrix} R_{ij} \\ G_{ij} \\ B_{ij} \end{bmatrix}, \tag{1}$$

where *R, G, B* are values in term of the original primaries. It can also be expressed as

$$\mathbf{C}'_{ij} = \begin{bmatrix} R'_{ij} \\ G'_{ij} \\ B'_{ij} \end{bmatrix}, \tag{2}$$

where R_{ij}', G_{ij}' and B_{ij}' are values in term of the new uncorrelated primaries. Thus, G_{ij}' is related to C_{ij} by a transformation matrix T:

$$\mathbf{C}'_{ij} = \mathbf{T}\mathbf{C}_{ij} \tag{3}$$

the covariance of the pixel data $\Sigma_{\mathbf{C}'_{ij}}$ is defined as

$$\begin{aligned} \Sigma_{\mathbf{C}'} &= \frac{1}{I \cdot J} \sum_{i=1}^{I} \sum_{j=1}^{J} (\mathbf{C}'_{ij} - \mathbf{m}_{\mathbf{C}'_{ij}})(\mathbf{C}'_{ij} - \mathbf{m}_{\mathbf{C}'_{ij}})^t \\ &= \varepsilon\left\{ (\mathbf{C}'_{ij} - \mathbf{m}_{\mathbf{C}'_{ij}})(\mathbf{C}'_{ij} - \mathbf{m}_{\mathbf{C}'_{ij}})^t \right\} \end{aligned} \tag{4}$$

where $\mathbf{m}_{\mathbf{C}_{ij}}$ is the mean vector of the image data in terms of the new primaries,

$$\mathbf{m}_{C_{ij}} = \frac{1}{I \cdot J} \sum_{i=1}^{I} \sum_{j=1}^{J} C_{ij}. \tag{5}$$

since

$$\mathbf{m}_{\mathbf{C}'_{ij}} = \varepsilon\left\{ \mathbf{C}'_{ij} \right\} = \varepsilon\left\{ \mathbf{T}\mathbf{C}'_{ij} \right\} = \mathbf{T}\varepsilon\left\{ \mathbf{C}_{ij} \right\} = \mathbf{T}m_{\mathbf{C}_{ij}}. \tag{6}$$

therefore

$$\begin{aligned} \sum_{\mathbf{C}'_{ij}} &= \sum_{\mathbf{C}'_{ij}} = \varepsilon\left\{ (\mathbf{C}'_{ij} - \mathbf{m}_{\mathbf{C}'_{ij}})(\mathbf{C}'_{ij} - \mathbf{m}_{\mathbf{C}'_{ij}})^t \right\} \\ &= \varepsilon\left\{ (\mathbf{T}\mathbf{C}_{ij} - \mathbf{T}\mathbf{m}\mathbf{C}_{ij})(\mathbf{T}\mathbf{C}_{ij} - \mathbf{T}\mathbf{m}\mathbf{C}_{ij})^t \right\} \\ &= \mathbf{T}\varepsilon\left\{ (\mathbf{C}_{ij} - \mathbf{m}\mathbf{C}_{ij})(\mathbf{C}_{ij} - \mathbf{m}\mathbf{C}_{ij})^t \right\} T^t \end{aligned}$$

i. e.,

$$\sum_{\mathbf{C}'_{ij}} = T \sum_{\mathbf{C}_{ij}^{Tt}} \tag{7}$$

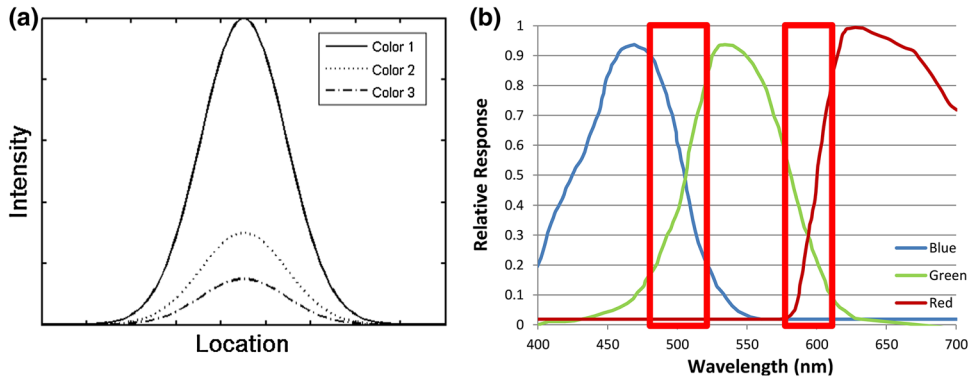

Fig. 4 Multiple exposures caused by signal bleed-through: **a** spectral response of a CCD sensor. The *black* rectangles show the overlap regions of the spectral response. **b** Multiple exposures from the same wavelength of light to different *color* channels. *Color* 1 is the response from the dominant wavelength

Since the new primaries are uncorrelated, $\Sigma_{\mathbf{C}'_{ij}}$ is diagonal. Thus, $\mathbf{T}$ is the transposed matrix of eigenvectors and $\mathbf{T}$ is an orthogonal matrix. Elements in $\Sigma_{\mathbf{C}'_{ij}}$ are the eigenvalues of $\Sigma_{\mathbf{C}'_{ij}}$.

The advantage of this method is that it is adaptive, so no parameter is required throughout the process, and the results are more robust to the variations of lighting. Figure 5 shows the result of color separation using the proposed algorithm. In the circled region, two green particles can be seen from both the green and blue channels before color separation, but after the color separation, only the new green channel keeps the two particle images.

2.4 Particle identification

The high magnification of the microscope optics with the pinhole configuration also changed the particle image size significantly. A typical particle image size from a 3D-μPTV image is around 25 pixels, since we are imaging a depth that extends beyond the focal plane; this is much larger than the 2–4 pixel diameter usually encountered in traditional 2D-PIV/PTV applications. As a result, the chance of a particle image overlap with another one increases drastically. Severe particle overlap would cause location errors of the peak and are critical to velocity measurement errors. To identify the particle image peak location more accurately, a particle identification algorithm, proposed by Lei et al. (2012), is used to improve the ability to identify overlap particle images. This is an algorithm modified from cascade correlation method (CCM), a particle identification method first proposed by Angarita-Jaimes et al. (2009). For completeness, the principle of the algorithm is described below.

Each PTV image can be considered as a superimposed intensity map of an unknown number N of individual particle images. Assuming a Gaussian shape distribution, each particle image has a different location, intensity and radius. Thus, the intensity $I(j, k)$ at pixel (j, k) is

$$\boldsymbol{I}(\boldsymbol{j},\boldsymbol{k}) = \sum_{i=1}^{N} (\boldsymbol{I}_0)_i \cdot \boldsymbol{e}^{-\frac{X_i(j,k)^2}{2r_i^2}}, \tag{8}$$

where $(I_0)_i$ is the peak intensity of the ith particle image, $X_i(j,k)$ is the distance from the pixel to the particle center (xc_i, yc_i), and r_i is the representative radius of the particle image. The particle identification process finds a solution

$$\boldsymbol{I}'^{(j,k)} = \sum_{i=1}^{N} (\boldsymbol{I}'_0)_i \boldsymbol{e}^{-\frac{X'_i(j,k)^2}{2r'^2_i}}, \tag{9}$$

so that the difference between $I(j, k)$ and $I'(j, k)$ for all pixels in the image is minimized in a least-square sense. The number of particles, N, in most particle identification algorithms is assumed to be equal to the number of peaks in the image, and $I(j, k)$ is independent for each particle i because the overlap between particle images is assumed to be negligible. Therefore, for each particle i, the equation can be reduced to

$$\boldsymbol{I}_i(\boldsymbol{j},\boldsymbol{k}) = \boldsymbol{I}_i \boldsymbol{e}^{-\frac{X'_j(j,k)^2}{2r'^2_j}}. \tag{10}$$

The intensity peaks for severely overlapping particles may merge together. It is therefore important to be able to accurately estimate N. This can be done by counting the number of peaks using the CCM algorithm. The CCM algorithm initially calculates the cross-correlation image R_1 between the original particle image I and the model particle mask image I_M,

$$\boldsymbol{R}_1(\boldsymbol{u},\boldsymbol{v}) = \frac{\sum_{i=u-m/2}^{u+m/2}\sum_{j=v-n/2}^{v+n/2}(\boldsymbol{I}(\boldsymbol{i},\boldsymbol{j})-\bar{\boldsymbol{I}})(\boldsymbol{I}_{\mathbf{M}}(\boldsymbol{i},\boldsymbol{j})-\bar{\boldsymbol{I}}_{\mathbf{M}})}{\sqrt{\sum_{i=u-m/2}^{u+m/2}\sum_{j=v-n/2}^{v+n/2}(\boldsymbol{I}(\boldsymbol{i},\boldsymbol{j})-\bar{\boldsymbol{I}})^2}\sqrt{\sum_{i=u-m/2}^{u+m/2}\sum_{j=v-n/2}^{v+n/2}(\bar{\boldsymbol{I}}_{\mathbf{M}}(\boldsymbol{i},\boldsymbol{j})-\bar{\boldsymbol{I}}_{\mathbf{M}})^2}}, \tag{11}$$

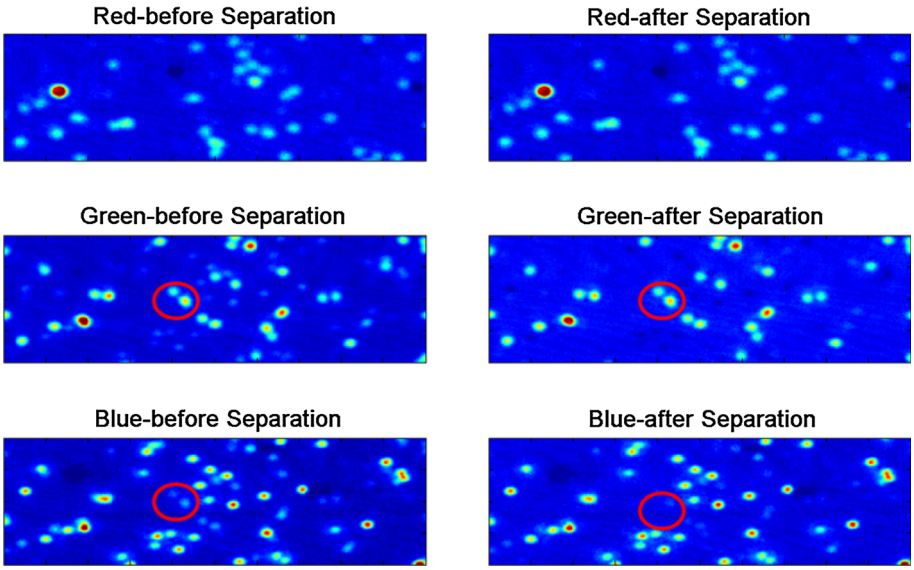

Fig. 5 Results of *color* separation algorithm

where the model particle mask image is defined as an intensity image of size $m \times n$ containing a particle image with a Gaussian shaped intensity profile which follows Eq. (10). The cross-correlation operation is then repeated to generate a cascade correlation image, R_2, by replacing I in Eq. (10) with the correlation image, R_1, and reducing the particle mask image radius r to 1 pixel. In performing this operation, the overlapping particle image can be separated effectively and is robust against intensity variations between the overlapping particles (Angarita-Jaimes et al. 2009). The cross-correlation operation in Eq. (11) can repeat k times, and each time the model particle mask image radius (the representative radius r) is reduced by 1 pixel until it reaches a user determined minimum radius, which is usually the lower limit of the particle image radius observed in the experiment. The number of peaks, N, is calculated by counting the local maxima in the last correlation plane, R_k, which are greater than a threshold value. Once N is estimated, a nonlinear least-square fit is performed by minimizing χ^2:

$$\chi^2 = \sum_{j=1,j=1}^{j=m,k=n} \left[I(j,k) - \sum_{i=1}^{N} (I_0)_i \cdot e^{-\frac{X_i(j,k)^2}{2r_i'^2}} \right]^2 . \quad (12)$$

By solving the least-square fit problem, the location (x_i, y_i), intensity $(I_0)_i$ and radius r_i of each of the particles in each blob can be found. In the original CCM algorithm, the peak locations in the R_2 plane are used to indicate the particle locations. In the present method, the number of peaks, N, is counted instead. With the value of N identified in Eq. (8), the least-square fitting can be performed to find the best estimate of the particle locations in the original image.

In practice, the whole image is broken into small sections (blob images) to reduce the computational cost without sacrificing accuracy. Each blob image contains an unknown number of particles and considered as an independent image described by Eq. (8). The particles in each blob are then identified using the procedure described above and repeated until all the blobs are processed. The final result is the summation of all the blob results. The block diagram for the whole procedure is shown in Fig. 6.

2.5 Particle location calculation

For the 3D-μPTV system, the chromatic aberration also causes equilateral triangle patterns to be seriously skew (Fig. 7). Thus, the characteristic equations derived in the DDPIV systems [Tien et al. (2008), Kajitani and Dabiri (2005), Grothe et al. (2008)] do not describe this system. This affects both the triplet finding and particle location calculations, since in the previous work both processes rely on the DDPIV characteristic equations. Thus, a calibration-based method is developed to first match the triplet particle images of a particle from each color channel, and then the particle location in physical space is calculated based on the calibration results.

The current system can be considered as a system with three pinhole camera views, as each color image plane formed from the color-coded pinhole can be considered as a distinct pinhole camera view. All of the two pinhole combinations are similar and sufficient to determine the particle location, but using three pinholes can greatly reduce the ambiguity of matching the image exposures from different image planes. Figure 8a shows a general case of the epipolar geometry of two pinhole camera views. This is representing any two pinhole image planes formed from the three pinholes. An epipolar line is the projection of a line of sight from one image plane onto another image

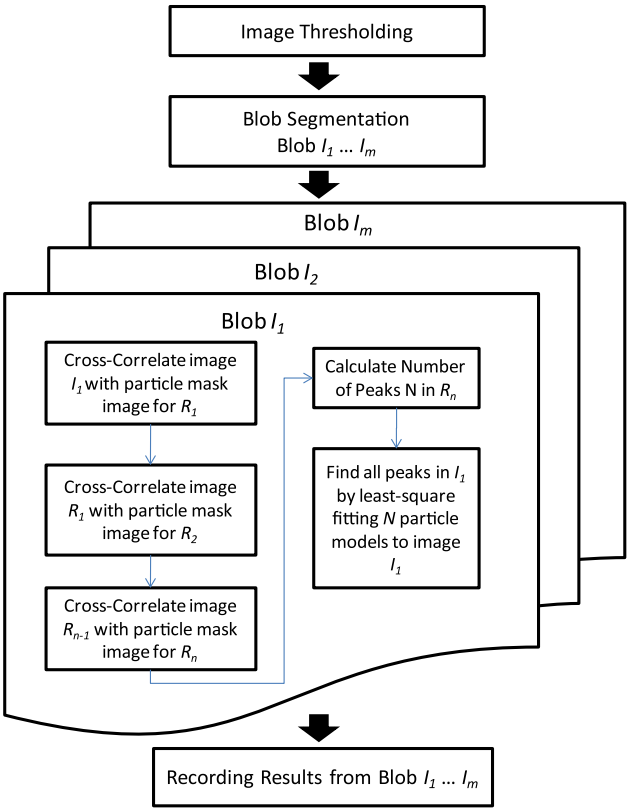

Fig. 6 Process flow of the proposed particle identification algorithm

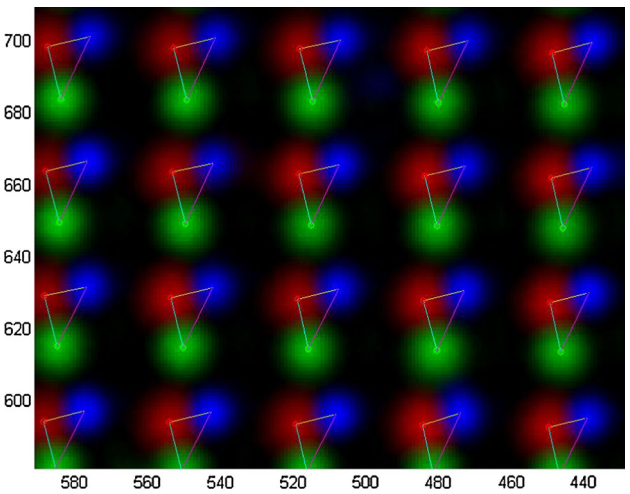

Fig. 7 Skewed *triangle* pattern of the triplet exposures due to chromatic aberration

plane. For instance, in Fig. 8a, the epipolar line $e_{L\text{-}R}$ can be found by projecting the line of sight $O_L P_1$ in the left image plane onto the right image plane. Particle image x_{L1} on the left plane particle could be formed from particle P_1, P_2 or P_3, but in the right image plane, it becomes distinct particle image x_{r1}, x_{r2} and x_{r3}, all falls on the same epipolar line $e_{L\text{-}R}$. By searching along the epipolar lines from different image planes, the particle image triplet of a particle can be determined. This is the epipolar line search method proposed by Maas et al. (1993) and applied to the current 3D-μPTV system to find the triplet match. The calculation of line of projections requires a full optical model of the system. The optical system is usually approximated by a pinhole camera model, and the camera parameters are found through a calibration procedure (Maas et al. 1993). However, due to the high magnification and larger depth of field with the pinhole, the accuracy of the simple pinhole model is not enough and the ability to correct image distortion at different depths is important. Thus, we model the optical system of the 3D-μPTV by developing a calibration-based procedure that is similar to Maas' epipolar line search method.

The calibration procedure is explained by Fig. 8b. A target plate with an array of dots is set to move to different positions. At each position, the calibration images are taken with the left and right cameras. Each calibration image is processed through the peak-finding algorithm introduced in Sect. 2.4 to find the projected peak locations. The projected peak locations from each image plane and the true physical positions of the calibration dots can be related by mapping functions

$$\begin{aligned} x_R &= f_{x,L\Rightarrow R}(x_L, y_L, Z) \quad y_R = f_{y,L\Rightarrow R}(x_L, y_L, Z) \\ x_L &= f_{x,R\Rightarrow L}(x_R, y_R, Z) \quad y_L = f_{y,R\Rightarrow L}(x_R, y_R, Z) \end{aligned} \tag{13}$$

$$\begin{aligned} X &= F_{X,L\Rightarrow XYZ}(x_L, y_L, Z) \quad Y = F_{Y,L\Rightarrow XYZ}(x_L, y_L, Z) \\ X &= F_{X,R\Rightarrow XYZ}(x_R, y_R, Z) \quad Y = F_{Y,R\Rightarrow XYZ}(x_R, y_R, Z) \end{aligned} \tag{14}$$

where (X, Y, Z) are the physical coordinates of the dot, (x_L, y_L) are the image coordinates of the projected peak location in the left image plane and (x_R, y_R) are the image coordinates of the projected peak location in the right image plane. The functions are approximated with radial basis functions (RBF, please refer to the "Appendix") written in a MATLAB routine by Chirokov (2012), and same procedure is performed for each pinhole pair (red to green, green to blue and blue to red). Once these functions are built, epipolar line can be created for any point in the image plane with Eq. (3). For triplet matching procedure, Eq. (4) is used for calculating the particle locations in experiments.

In the actual experiment, once the image triplets of a particle are matched by the epipolar line search method, the next step is to calculate the physical coordinates of the particle location (X_p, Y_p, Z_p) based on the peak image coordinates (x_r, y_r)(x_g,y_g) and (x_b,y_b) of red, green and blue pinhole, respectively. The Z coordinate is first to be found from Eq. (3). It is calculated iteratively by a minimum search routine based on a derivative-free method. Once the Z coordinate is found, Eq. (4) is used to calculate the X and Y coordinates of the particle location. Only two of the peak locations are necessary, but all three pinhole pairs (red to

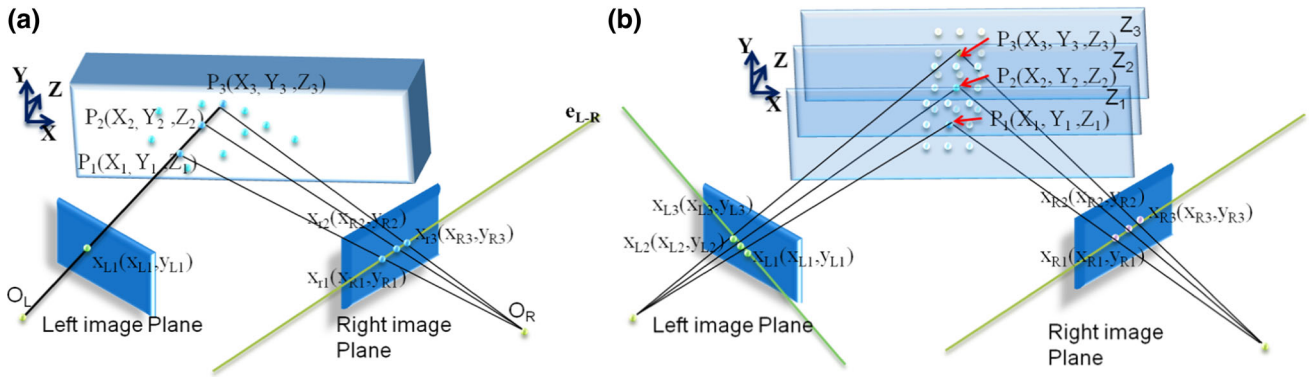

Fig. 8 **a** Epipolar geometry, **b** calibration procedure

green, green to blue and blue to red) are used to get the coordinates, and the average values are used to improve the accuracy.

2.6 Particle tracking

After particle locations from two time frames are found, the last processing stage of the 3D-μPTV system is to find the velocity field. In the current work, the particle tracking algorithm, based on the original Scott and Longuet-Higgins (1991) method, is an adaptation of our previous work (Lei et al. 2012), but expand it from 2D to 3D. The implementation of the method is hybridized with PIV results, and an iterative scheme with outlier detection method by Duncan et al. (2010) is used to increase the robustness and accuracy of the method. The guiding 3D-PIV field is built using a 3D cross-correlation method developed by Pereira et al. (2000).

3 Experimental setup

3.1 Hardware setup

The 3D-μPTV system is developed and tested based on the principles introduced in the previous section. Figure 9 shows a schematic of the current 3D-μPTV system setup. To demonstrate the capability of the system, a micro-scale backward-facing step flow is set up and the flow field is resolved by the 3D-μPTV system. The experimental apparatus consists of four major components: the infinity-corrected inverted microscope system, the micro-channel flow system, the calibration system and the data processing software.

Since the 3D-μPTV system is designed to measure fluid flow in micro-scales, the requirement for magnification (usually > 10) makes the microscope system a critical component of the system. In order to have more flexibility

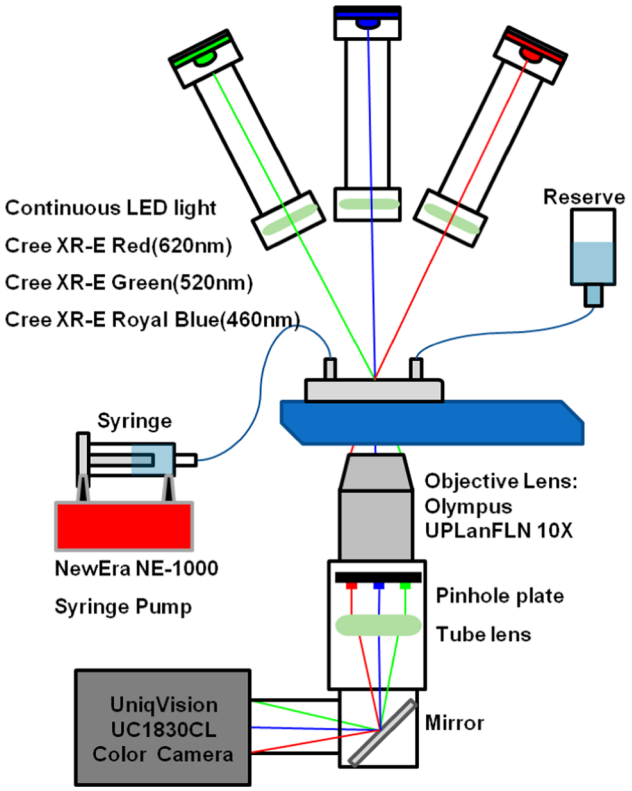

Fig. 9 Schematic of 3D-μPTV experimental setup

to test different optical configurations, a customized inverted microscope system is designed and assembled. As shown in Fig. 9, the lights are set on top and the objective lens is put underneath the flow model. The main reason to choose the inverted configuration is for the ease of testing different lighting configurations, and it also provides an easy access for aligning the calibration target and micro-channel model, since it has a longer working distance to the light source In the current setup, both the objective lens (Olympus UPLanFLN 10X) and the tube lens (U-TLU) are made by Olympus to insure the optical performances are

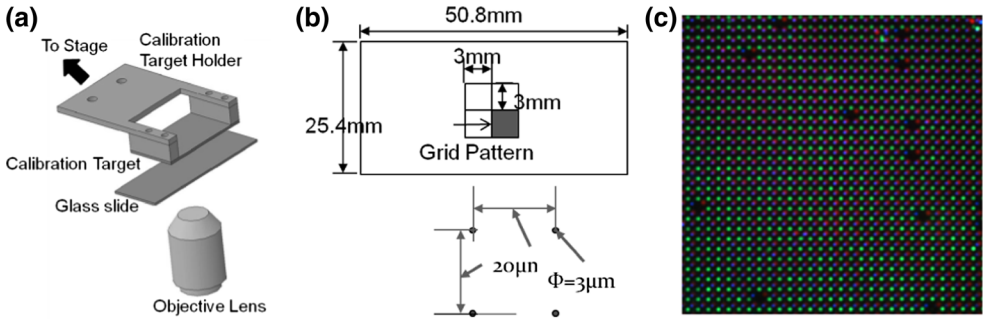

Fig. 10 System calibration: **a** experimental setup, **b** target plate pattern, **c** example of a calibration image

matched. Due to the additional length of the adapter ring for the camera mounting, the actual magnification measured from the image of a target plate is 10.965 instead of 10.

The three-pinhole plate is placed in the objective lens right after the lens elements. The diameter of each pinhole is $d = 1.5$ mm, and the distance R (from the pattern center to each pinhole center) is 3 mm, results in a pinhole separation distance of 5.196 mm. The current configuration results in a measurable image volume of 600 × 600 × 600 μm^3.

High power LEDs (light-emitting diode) are used as the light source of the system. Compared with other incoherent light sources, the main advantage of LEDs is that they have the narrow spectral widths. The spectral width (full width at half maximum, FWHW) of a typical quasi-monochromatic LED varies from 20 to 40 nm, which is ideal to match the spectral response of those pinhole color filters. In the current system, three Cree XR-E series LEDs with Red (620 nm), Green (520 nm) and Royal Blue (460 nm) are used to provide a continuous light source. Critical illumination configuration is used where each LED is aligned with a lens doublet to focus the light to the object plane. A 1,024 pixel × 1,024 pixel resolution color CCD camera (uniqvision UC-1830CL) of a frame rate of 30 frame per second is used to capture the images. The typical exposure time is set to 4.167 ms (1/240 s). The data rate is 30 Hz. Images are captured and recorded by software (Video Savant® 4, IO Industries Inc.) through a frame grabber board (Road Runner R3 CL, Bitflow Inc.) in a PC.

3.2 System calibration

A calibration apparatus is constructed to perform the calibration procedure presented in Sect. 2.5. As shown in Fig. 10a, the calibration target is a 50 mm × 25 mm × 1.52 mm glass plate with grid arrays of blue chrome dots. The size of each dot is 3 μm with a grid spacing of 20 μm (Fig. 10b). The target plate is connected to a 6-axis translation stage (APT 600, Thorlabs). The stage is used to align

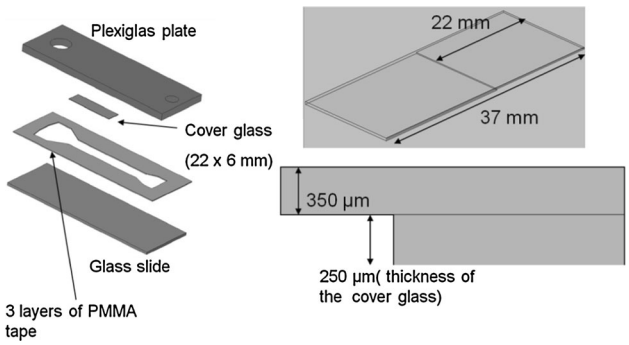

Fig. 11 Backward-facing step micro-channel

the calibration target with the optical axis of microscope system to provide the accurate position in Z-axis of the target for each calibration plane. A glass slide of the same size to the bottom glass plate used for the micro-channel model is put in between the objective lens and the calibration target. By putting water in between the glass slide and the target plate, the refraction effect of water the glass material is matched this way during calibration. A total of 14 planes data are taken, with 25 μm spacing in the Z-axis. The focal plane is set to the mid-plane of the 14 calibration planes and centered around the step so that the measurable volume covers the whole micro-channel. Figure 10c shows a typical calibration image taken during the calibration test.

A backward-facing step flow micro-channel is constructed to test the performance of the 3D-μPTV system (Fig. 11). A piece of 22 mm × 6 mm × 0.2 mm thin glass plate cut from a cover glass is glued to a 75 mm × 25 mm glass slide to form the step of the flow channel. The top wall is a transparent plexiglas plate cut to the same size as the bottom glass slide and glued together by double-sided PMMA (Poly (methyl methacrylate)) tape and a thin layer of epoxy glue. The tape and glue are also served as the side walls of the micro-channel. Both the top and bottom walls are transparent to ensure clear optical access for lighting the volume of interest. The resulting channel dimension is 22 mm × 6 mm × 0.35 mm before the step and 15 mm × 6 mm × 0.6 mm after the step. The laminar

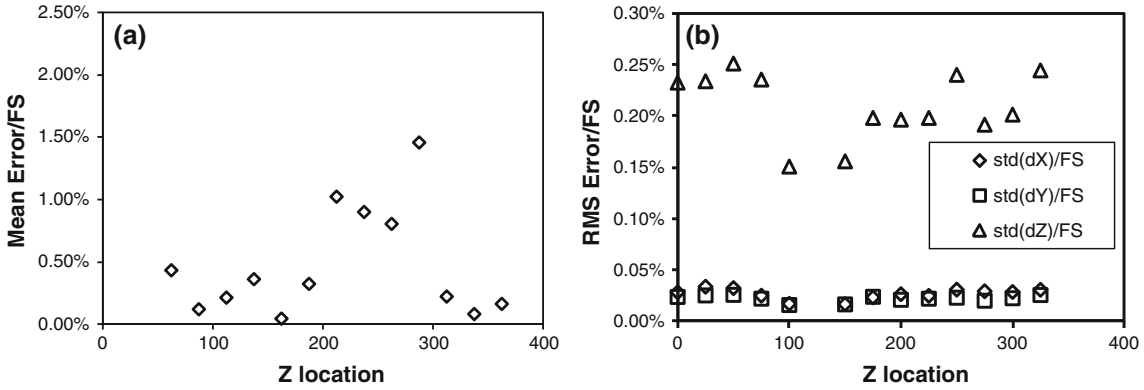

Fig. 12 Location error test results: **a** Mean error, **b** RMS error

flow is driven by a syringe pump (NewEra NE-1000), and deionized (DI) water is used as the working fluid. 2 μm polystyrene particles (Polybead® Microspheres, Polysciences Inc.) are used as the tracer particles.

The data processing software is coded in MATLAB (Mathworks, Natick, MA). Video captured by the data recording software is saved in individual frames in 24-bit color image format, and the final data output is the particle locations in physical space.

3.3 Measurement uncertainty

To test the accuracy of the 3D-μPTV system, an experiment is conducted using the calibration apparatus described in the previous section. The calibration target is moved by the translation stage by a known amount, and images are taken before and after the movement. Then, the images of the dots are processed as if they are the actual particles, and tracking is performed to find out the displacement of each dot. Since the locations of the dots on the target are known, the accuracy of the system can be estimated. The advantage of this approach is the ability to estimate the accuracy of the system closest to the actual experimental conditions, because all measurement errors other than that introduced by the flow system are reflected to the results. Since the present work is using the photogrammetric imaging approach, the velocity is calculated from the displacement of each tracer particle between two frames, the location error directly contributes to the final velocity error. Thus, the location error is estimated from each image and the displacement error is calculated using the image pairs.

The location errors are estimated in two ways: the mean error and the standard deviation. The errors are also sorted to two different groups: the in-plane error and out-of-plane error. The in-plane error represents errors in the X and Y directions, which is parallel to the image plane, and out-of-plane errors represent the error in the Z direction, which is along the optical axis. The calibration target is moved in the Z direction by increments of 25 μm as the procedure as described in the calibration section, except the dots are shifted away from the calibration locations. The image is taken and processed with the processing discussed in the previous chapters. The mean error is estimated by comparing to the Z readings of the translation stage. Figure 12a shows the mean error with normalization throughout the calibration range ($Z = 0$–325 μm). It is shown that the mean error is lower than 1.5 % of the full calibration range, which corresponds to a variation from 0.09 to 3.96 μm.

The in-plane root mean square (RMS) error is estimated by comparing the calculated dot positions at different Z locations to those on a model plane. Figure 12b shows both the normalized in-plane (X and Y) and out-of-plane errors. The in-plane variations are both less than 0.05 %, while the out-of-plane error is around 0.25 %, which correspond to 0.16 and 0.81 μm, respectively.

To test for the displacement error, the target is moving by the translation stage in all three axes with a increments of 10 μm for the in-plane and out-of-plane tests. The mean and standard deviation of the error of displacement are calculated and shown as Fig. 13. Both the mean and standard deviation of the errors are lower than 1 % of the full measurement range, which are on the same level with the location error. This result indicates the accuracy of the 3D-μPTV system is high and uniform throughout the field of view, since with large displacement up to 50 μm (8 % of the length of view), the error is still low.

4 Experimental results

The true test of the performance of 3D-μPTV system is of course to resolve a real flow case. The backward-facing step flow micro-channel is used for this purpose. The main advantage of the 3D-μPTV system based on the color-coded pinhole system is the possibility to increase the particle density. Most of the current 3D techniques are

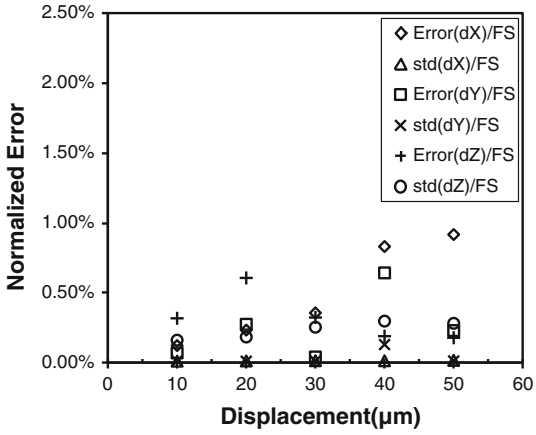

Fig. 13 Displacement error

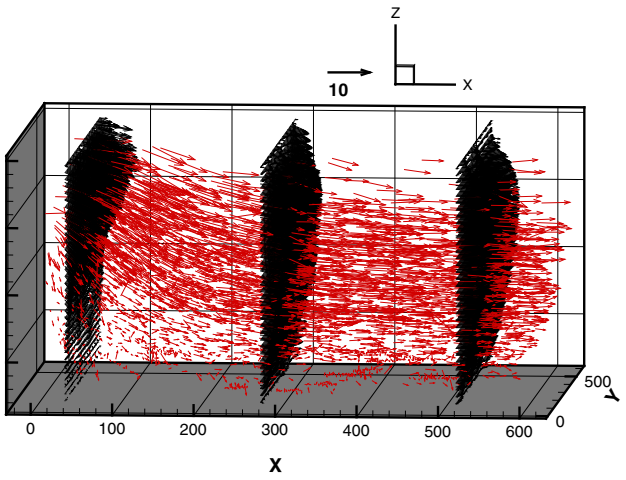

Fig. 14 Resolved backward-facing step flow field: steady flow

limited to low particle density; as a result, they have to rely on time-averaging to get enough data to resolve the whole flow field and the consequence is that the flow field has to be steady. Thus, it is important to test whether the proposed new technique can be used to break this limitation.

4.1 Steady flow

The first experiment is to verify the system performance with a steady flow. Using the setup presented in section F, the flow is maintained at 40 μl/min which corresponds to a Reynolds number Re = 0.22. The field of view is located right after the backward-facing step with an imaged volume of 600 × 600 × 600 μm^3. One hundred and fifty six image pairs are processed and the results are overlapped to one field, as shown in Fig. 14. (red vectors). A total of 20,592 vectors are identified, indicating an average of 132 vectors per image pair. Using RBF interpolation (please refer to the "Appendix" section), the PTV result is interpolated to a uniform grid spacing on the size of 10 μm × 10 μm × 10 μm, as shown in Fig. 14 (Black vectors, only showing the representative planes). The flow field result clearly shows the flow structure after the step with high spatial resolution.

4.2 Unsteady flow

The second experiment is to explore the possibility to use only one image pair to resolve the flow field with reasonable spatial resolution for a unsteady flow. The unsteady backward-facing step flow is created by decelerating the constant flow rate at 150 μl/min by 12 step decrements at 12 μl/min, resulting in the Reynolds number changing from 0.825 to 0.033. The imaged volume is 600 × 600 × 600 μm^3, as in the steady flow case. The syringe and the tubing provide a damping effect, so the flow is decelerating smoothly without step change.

Figure 15a shows the vector field using particle tracking results from the starting frame pair (Q = 150 μl/min). A total of 392 vectors are identified in an image pair, shown in the red vectors, and the corresponding interpolated vector field (black vectors) on a uniform grid of size of 40 μm × 40 μm × 30 μm. The spatial resolution is lower than the time-averaged case, but the flow features are still captured extremely well. Figure 15b shows the vector field of particle tracking results from the ending frame pair (Q = 6 μl/min). A total of 444 vectors are identified in a image pair, shown in the red vectors, and the corresponding interpolated vector field (black vectors) on a uniform grid of size of 40 μm × 40 μm × 30 μm. These results indicate that the unsteady flow can be resolved with our 3D-μPTV technique.

5 Conclusion

A novel three-dimensional micro particle tracking velocimetry technique is developed using a single color camera. By modifying the illumination method and adopting several new processing algorithms, this 3D micro particle tracking velocimetry is able to measure a flow inside a 600 μm × 600 μm × 600 μm volume with high spatial and temporal resolution. A micro-scale backward-facing step flow is resolved in both steady and decelerating flow conditions, ranging from Reynolds number 0.825 to 0.033. These results show that the proposed technique is able to capture micro-scale flow with high spatial resolution in a cubic volume, which provides the technique to capture larger three-dimensional flow structure than other 3D techniques. This technique also achieves a high enough particle image density that can provides necessary temporal resolution to resolve unsteady flow.

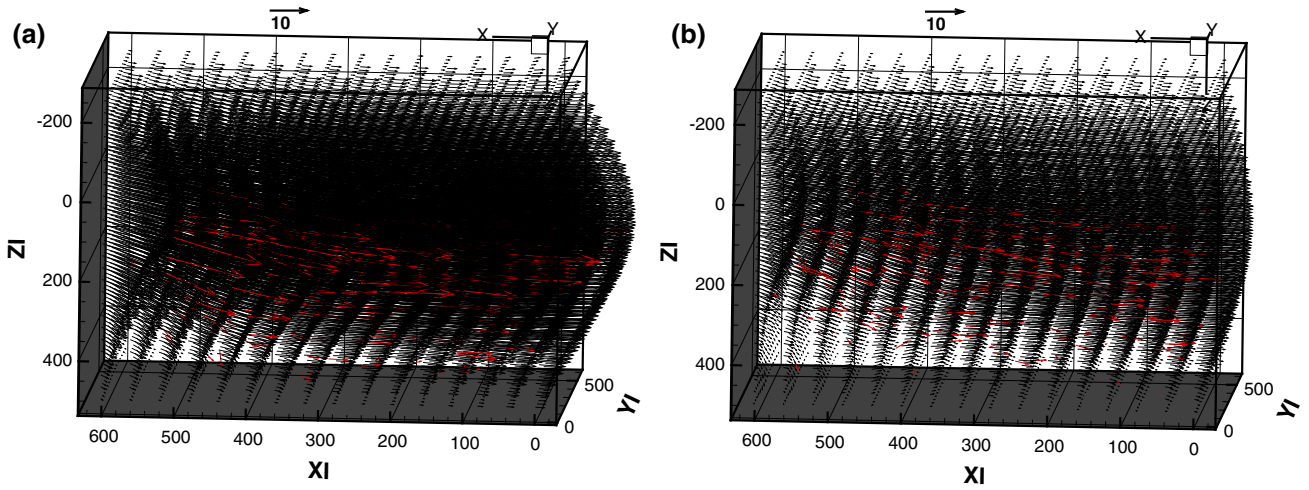

Fig. 15 Resolved backward-facing step flow field: decelerating flow at (**a**) the start (**b**) at the end

Acknowledgments The authors gratefully acknowledge the support of the National Institutes of Health (R01 RR023190-04) and the Murdock Trust Foundation.

Appendix

The radial basis function (RBF) interpolation is a method for approaching a function with given data points. The RBF is a real-valued function depending only on the distance from a certain point,

$$\varphi(r) = \varphi(||x - x_i||), \tag{15}$$

where $r = (||x - x_i||)$ is the Euclidean distance in the current work.

For N given points, the target function can be approximated by the sum of N radial basis function,

$$f(x) = c_0 + c_1 x + \sum_{i=1}^{N} \lambda_i \varphi(|x - x_i|), \tag{16}$$

where the coefficients c_0, c_1, and λ_i are chosen to match the function values at the known data points (interpolation nodes). Because the approximation function is linear to the coefficients, these coefficients can be estimated using matrix methods of linear least squares. Several basis functions can be used are listed below:

Gaussian:

$$\varphi(r) = \exp\left(-\frac{r^2}{2\sigma^2}\right), \tag{17}$$

Multiquadrics:

$$\varphi(r) = \exp\sqrt{\left(1 + \frac{r^2}{\sigma^2}\right)}, \tag{18}$$

Linear:

$$\varphi(r) = r, \tag{19}$$

Cubic:

$$\varphi(r) = r^3, \tag{20}$$

Thinplate:

$$\varphi(r) = \ln(r + 1) \tag{21}$$

once coefficients c_0, c_1,and λ_i are found, this expression can be used to estimate value of the function at any point.

References

Adrian RJ, Westerweel J (2011) Particle image velocimetry. Cambridge University Press, Cambridge

Angarita-Jaimes NC, McGhee E, Chennaoui M, Campbell HI, Zhang S, Towers CE, Greenaway AH, Towers DP (2006) Wavefront sensing for single view three-component three-dimensional flow velocimetry. Exp Fluids 41(6):881–891

Angarita-Jaimes NC, Roca MAG, Towers CE, Read ND, Towers DP (2009) Algorithms for the automated analysis of cellular dynamics within living fungal colonies. Cytom Part A 75A(9):768–780

Bown MR, MacInnes JM, Allen RWK, Zimmerman WBJ (2006) Three-dimensional, three-component velocity measurements using stereoscopic micro-PIV and PTV. Meas Sci Technol 17(8):2175–2185

Chen S, Angarita-Jaimes N, Angarita-Jaimes D, Pelc B, Greenaway AH, Towers CE, Lin D, Towers DP (2009) Wavefront sensing for three-component three-dimensional flow velocimetry in microfluidics. Exp Fluids 47(4–5):849–863

Chirokov A (2012) Scattered data interpolation and approximation using radial base functions. http://www.mathworks.com/matlabcentral/fileexchange/10056-scattered-data-interpolation-and-approximation-using-radial-base-functions

Cierpka C, Segura R, Hain R, Kaehler CJ (2010) A simple single camera 3C3D velocity measurement technique without errors

due to depth of correlation and spatial averaging for microfluidics. Meas Sci Technol 21(4):045401

Cierpka C, Rossi M, Segura R, Kaehler CJ (2011) On the calibration of astigmatism particle tracking velocimetry for microflows. Meas Sci Technol 22(1):015401

Duncan J, Dabiri D, Hove J, Gharib M (2010) Universal outlier detection for particle image velocimetry (PIV) and particle tracking velocimetry (PTV) data. Meas Sci Technol 21(5): 057002

Grothe R, Rixon G, Dabiri D (2008) An improved three-dimensional characterization of defocusing digital particle image velocimetry (DDPIV) based on a new imaging volume definition. Meas Sci Technol 19:065402

Kajitani L, Dabiri D (2005) A full three-dimensional characterization of defocusing digital particle image velocimetry. Meas Sci Technol 16(3):790–804

Lei Y, Tien W, Duncan J, Paul M, Dabiri D, Rösgen T, Hove J (2012) A vision-based hybrid particle tracking velocimetry (PTV) technique using a modified cascade-correlation peak-finding method. Exp Fluids 53(5):1251–1268

Lindken R, Westerweel J, Wieneke B (2006) Stereoscopic micro particle image velocimetry. Exp Fluids 41(2):161–171

Luo R, Sun Y (2011) Pattern matching for three-dimensional tracking of sub-micron fluorescent particles. Meas Sci Technol 22(4):045402

Luo R, Yang XY, Peng XF, Sun YF (2006) Three-dimensional tracking of fluorescent particles applied to micro-fluidic measurements. J Micromech Microeng 16(8):1689–1699

Maas HG, Gruen A, Papantoniou D (1993) Particle tracking velocimetry in 3-dimensional flows. 1. Photogrammetric determination of particle coordinates. Exp Fluids 15(2):133–146

Ooms TA, Lindken R, Westerweel J (2009) Digital holographic microscopy applied to measurement of a flow in a T-shaped micromixer. Exp Fluids 47(6):941–955

Park JS, Kihm KD (2006) Three-dimensional micro-PTV using deconvolution microscopy. Exp Fluids 40(3):491–499

Pereira F, Gharib M (2002) Defocusing digital particle image velocimetry and the three-dimensional characterization of two-phase flows. Meas Sci Technol 13(5):683–694

Pereira F, Gharib M, Dabiri D, Modarress D (2000) Defocusing digital particle image velocimetry: a 3-component 3-dimensional DPIV measurement technique. Application to bubbly flows. Exp Fluids 29:S78–S84

Pereira F, Lu J, Castano-Graff E, Gharib M (2007) Microscale 3D flow mapping with mu DDPIV. Exp Fluids 42(4):589–599

Peterson SD, Chuang H, Wereley ST (2008) Three-dimensional particle tracking using micro-particle image velocimetry hardware. Meas Sci Technol 19(11):115406

Richards JA, Jia X (1999) Remote sensing digital image analysis: an introduction. Springer, Berlin

Santiago J, Wereley S, Meinhart C, Beebe D, Adrian R (1998) A particle image velocimetry system for microfluidics. Exp Fluids 25(4):316–319

Satake S, Kunugi T, Sato K, Ito T, Kanamori H, Taniguchi J (2006) Measurements of 3D flow in a micro-pipe via micro digital holographic particle tracking velocimetry. Meas Sci Technol 17(7):1647–1651

Scott GL, Longuet-higgins HC (1991) An algorithm for associating the features of 2 images. Proc R Soc Lond Ser B Biol Sci 244(1309):21–26

Sheng J, Malkiel E, Katz J (2006) Digital holographic microscope for measuring three-dimensional particle distributions and motions. Appl Opt 45(16):3893–3901

Tien W-H, Kartes P, Yamasaki T, Dabiri D (2008) A color-coded backlighted defocusing digital particle image velocimetry system. Exp Fluids 44(6):1015–1026

Towers CE, Towers DP, Campbell HI, Zhang SJ, Greenaway AH (2006) Three-dimensional particle imaging by wavefront sensing. Opt Lett 31(9):1220–1222

Willert CE, Gharib M (1992) Three-dimensional particle imaging with a single camera. Exp Fluids 12:353–358

Yoon SY, Kim KC (2006) 3D particle position and 3D velocity field measurement in a microvolume via the defocusing concept. Meas Sci Technol 17(11):2897–2905